NEW METHOD OF PHOTOMETRIC CORRECTION FOR LUNAR UVVIS IMAGES. Y. Yokota[1], R. Honda[2], Y. Iijima[1], and H. Mizutani[1], [1]Institute of Space and Astronautical Science (3-1-1 Yoshinodai, Sagamihara, Kanagawa 229-8510, Japan; yokota@planeta.sci.isas.ac.jp), [2]Kochi University, Japan.

Introduction: An accurate phase function is necessary for precise photometric correction of the Clementine lunar UVVIS images. Although several researchers have proposed photometric models for Clementine UVVIS images using empirical phase functions (e.g., [1] [2] [3]), additional work is required for correction of the data at small phase angle (<20°), because the phase function at small phase angle is significantly dependent on both the wavelengths and the geology. We propose the iterative method of photometric correction, in which automatic clustering of multi-band spectrum by Self-Organizing Map (SOM) [4] method, and determination of phase function for each spectral group are successively performed.

Basic Photometric model: Viewing geometry at lunar surface is specified with three angles: incidence angle i, emission angle e, and phase angle α, and i=30°, e=0°, and α=30° are generally employed as the standard viewing geometry.

We employed the lunar photometric model expressed by

$$I_\lambda(x,y;i,e,\alpha) = C_\lambda R_{30,\lambda}(x,y) D(i,e,\alpha) F_{\lambda,k}(\alpha) \quad , \quad (1)$$

where λ is the wavelength, x and y denote the position on the lunar surface, $I_\lambda(x, y; i, e, \alpha)$ is DN of the observed intensity of light, C_λ is the unit transformation coefficient, $R_{30,\lambda}$ is the bidirectional reflectance at the standard viewing geometry, $D(i, e, \alpha)$ is a function of incidence and emission angles, k denotes the geological group of the lunar surface, and $F_{\lambda k}(\alpha)$ is the phase function. We use $D(i, e, \alpha)$ and phase function in the normalized form as $D(\alpha, 0°, \alpha)$=1 and $F_{\lambda k}(30°)$=1. The function $D(i, e, \alpha)$ is transformed the function $X_L(i, e, \alpha)$ of [1] by the following equation:

$$D(i,e;\alpha) = X_L(i,e,\alpha) / X_L(\alpha,0°,\alpha) \quad . \quad (2)$$

When the spacecraft observes the lunar surface at the standard viewing geometry (30°, 0°, 30°) and at the non-standard viewing geometry (i_1, e_1, α_1), the phase function is expressed by

$$F_{\lambda k}(\alpha_1) = \frac{I_\lambda(x,y;i_1,e_1,\alpha_1)}{D(i_1,e_1,\alpha_1) I_\lambda(x,y;30°,0°,30°)} \quad . \quad (3)$$

Thus we can determine the phase function by the fit of the ratios between standard and non-standard geometry observation at various phase function α_1 [5]. To separate geological type dependence, we add the empirical adjustment function to the phase function as follows:

$$F_{\lambda k}(\alpha_1) = G_{\lambda k}(\alpha_1) F_{\text{standard}\lambda}(\alpha_1),$$

$$G_{\lambda k}(\alpha) = b_{\lambda k0} + b_{\lambda k1}\alpha + b_{\lambda k2}\alpha^2 + b_{\lambda k3}\alpha^3 + b_{\lambda k4}\alpha^4,$$

where $F_{standard\lambda}(\alpha)$ is the normalized function of the phase function proposed by [1], $G_{\lambda k}(\alpha)$ is the adjustment function that reflects material type dependence, and $b_{\lambda k0}$,..., $b_{\lambda k4}$ are the parameters determined by the fit of the dataset. The equation which corrects the reflectance is expressed by

$$R_{30,\lambda}(x,y) = R'_{30,\lambda}(x,y) / G_{\lambda k}(\alpha), \quad (4)$$

where $R'_{30,\lambda}$ is the initial reflectance derived from $F_{standard\lambda}(\alpha)$.

Data Processing: In analysis, we considered the equatorial area located in the latitude ranging from 30°N to 30°S and in the longitude ranging from 0°E to 360°E. We processed 114,208 Clementine UVVIS images (orbit 32-300) of 3 bands (415, 750, 950nm) in total.

All images are registered with the reference map of 750 nm mosaic image originated by USGS [6] by using a pattern matching of small craters and affine transforms. The original DN is calibrated using the hardware properties [7].

We tested the temporal sensitivity change of the camera by comparing two images that observed the same area at time interval of one month and under the same viewing geometry. There were 1.3-1.6% intensity differences between them, and we added the correction about these differences to the all data.

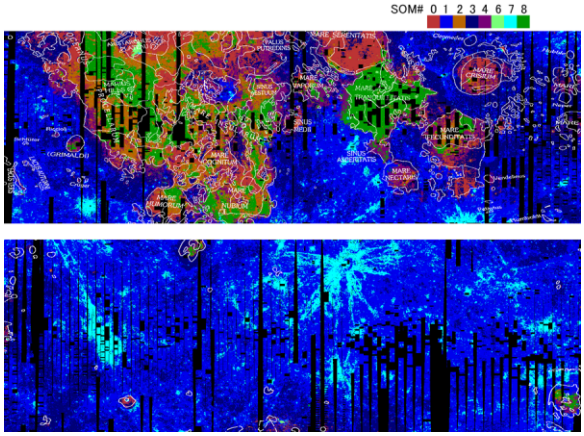

Figure 1. Distribution of spectrum group on lunar surface. The cluster IDs of the spectrum group (see Table 1) is displayed in a simple cylindrical map. Near side and far side of the moon are shown in the upper map and the lower map, respectively. Latitude ranges from 30°N to 30°S. Data lacking area is shown as black area. Boundaries of spectral unit map of [8] are superimposed as contours on the map.

Table 1. Geological interpretation for each spectral cluster.

SOM Group #	Interpretation
#0	Low & very low Ti mare. (Mare Serenitatis, Imbrium, etc.)
#1	Typical highlands.
#2	Relatively High Ti mare.
#3	Relatively low albedo highland. (KREEP or mixture with mare.)
#4	Mixture of mare & highland.
#5	(Some irregular data.)
#6	Immature mare materials.
#7	Immature highland materials.
#8	High Ti mare. (Mare Tranquillitatis, Procellarum, etc.)

In order to facilitate processing of overlapping data, image pixels were sampled as BINs of 0.1^o x 0.1^o squares, and their attributes such as the calibrated intensity, the wavelength, and the parameters of viewing geometry are stored in the database. Dataset of 1,907,278 BINs are successfully collected from 88% of the target area. The size of the database amounts up to 2.75 GB.

Automatic Clustering of the Spectrum and Phase Function Determination. Using the database, we selected 67,924 target BINs in which one image was observed under the standard viewing geometry （actually this condition was modified as the quasi-standard condition of $e \leq 10^o$ and $27^o \leq \alpha \leq 33^o$） and the other was observed under the non-standard viewing geometry.

Firstly, we calculate R'_{30} for all target BINs are calculated from the observation under quasi-standard geometry by using phase function of [1]. We assumed this value as the first approximation of R_{30} because the difference between R_{30} and R'_{30} must be very small at quasi-standard geometry.

Secondary, clustering of target BINs' 3-color R_{30} was performed. We employed the method of the Self-Organizing Map [4] for clustering of a large amount of multi-spectrum data. The Self-Organizing Map (SOM) is an unsupervised learning algorithm. SOM effectively maps the similarity of input vectors, thus it is commonly used to divide a large amount of high-dimensional data sets into a given number of groups and to visualize the result. We divided the target data into 9 groups by this method. Since one group consisted of irregular data after the clustering, we excluded this group from the analysis. Thus we used the data divided into 8 groups.

Finally, $F(\alpha)$ and thus $G(\alpha)$ are determined by the fit of each of 8 groups dataset.

Correction of the whole dataset. We utilize the obtained result of both clustering and phase function for correction of the rest of data in which no observation was made under the standard condition. We can obtain homogeneously corrected global lunar multi-spectral images as a result.

The data are photometrically corrected to R'_{30} by using phase function of [1]. Using the result of the clustering, each 3-color R'_{30} spectrum is classified as the cluster ID *#k*. The 3-color R'_{30} is photometrically corrected to R_{30} by using $G(\alpha)$ of cluster *#k*. Then, the classification is revalued by using the newly determined R_{30}. This procedure is iterated until the result is stabilized.

Experiments showed that discrepancies between R_{30} obtained from both observations of the standard viewing geometry and the non-standard viewing geometry were up to 10% after the first iteration. The disagreement reduced down to 4% after three times of iteration. This indicates the iterative process of clustering and phase function determination improved accuracy of phase function significantly.

Results: Figure 1 represents the obtained cluster ID (spectrum group) distribution on the lunar surface. Comparing the distribution with the lunar spectral unit map [8] and Lunar Prospector's FeO [9], TiO_2 [10], Th [11] data, we semantically indexed the obtained clusters to discuss difference of phase functions on the geological and petrological basis (Table 1). The results suggest that both highland and mare appear to be divided into finer groups characterized by maturity (the degree of exposure to the space) and composition. Figure 2 shows a comparison between $G(\alpha)$s of typical highland (#1) and high Ti mare (#8) at 750nm band, respectively. The normalized phase curves of highland are lower than the curve of mare at every band and at phase angles smaller than ~20^o. The difference increases with the increase of wavelength. The intensity difference between highland and mare increases up to 7.6 % at phase angle 6^o and at 950nm band. Since such a large difference cannot be ignored in lunar compositional study, individual phase function for each spectral group should be used for photometric correction of images observed at such low phase angles.

The variation of phase functions is also observed among the different mare (#0, #2, #8), among which the cluster #8 (High Ti mare) has the highest phase curves. The phase curves of other mare groups (#0:Low & very low Ti mare, #2: Relatively High Ti mare) are placed between the #8 and typical highland #1.

Among the highland clusters (#1 and #7), the $G(\alpha)$ of immature highland (#7) is slightly lower than that of mature highland (#1) with the difference of ~2.2% at the wavelength of 750nm and at the phase angle ranging from 5.0 to 6.0^o. The difference of $G(\alpha)$ between different maturity groups is smaller than the difference between compositionally different groups such as highland and mare.

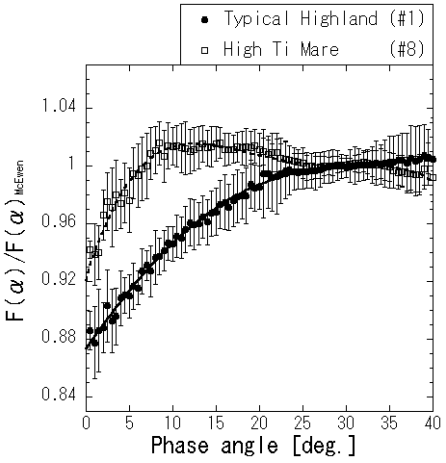

Figure 2. Comparison of the normalized phase functions between typical highland and high Ti mare at 750nm band.

References: [1] McEwen A. S. et al. (1998) *LPS XXIX*, Abstract #1466. [2] Hillier J. K. et al. (1999) *Icarus*, *141*, 205-225. [3] Kreslavsky M. A. et al. (2000) *JGR.*, *105 E8*, 20,281-20,295. [4] Kohonen T. (1995) *Self-Organizing Maps*, Springer Series in Information Sci., Vol 30. [5] Yokota Y. et al. (1999) *Adv. Space Res.*, *23*, 1841-1844. [6] Isbell C. E. et al. (1997) *LPS XXVII*, 623.[7] Malaret E. L. et al. (1998) *NASA NASW-5014.* [8] Wilhelms (1987) *The Geologic History of the Moon*, USGS professional paper 1348. [9] Lawrence D. J. et al. (2001) *LPS XXXII*, Abstract #1830. [10] Prettyman T. H. et al. (2002) *LPS XXXIII*, Abstract #2012. [11] Lawrence D. J. et al. (2002) LPS *LPS XXXIII*, Abstract #1970.